RECEIVED 2009 DECEMBER 21; ACCEPTED 2010 APRIL 5
Preprint typeset using LaTeX style emulateapj v. 11/10/09

FAR-INFRARED PROPERTIES OF *SPITZER*-SELECTED LUMINOUS STARBURSTS

A. KOVÁCS[1,2], A. OMONT[3,4], A. BEELEN[5], C. LONSDALE,[6,7], M. POLLETTA[7], N. FIOLET[3,4], T. R. GREVE[8,9], C. BORYS[10], P. COX[11], C. DE BREUCK[12], H. DOLE[5], C. D. DOWELL[10], D. FARRAH[13], G. LAGACHE[5], K. M. MENTEN[2], T. A. BELL[10], F. OWEN[14]
[1]University of Minnesota, 116 Church St SE, Minneapolis, MN 55414, USA
[2]Max-Plank-Institute für Radioastronomie, Auf dem Hügel 69, 53121 Bonn, Germany
[3]UPMC Univ Paris 06, UMR7095, Institut d'Astrophysique de Paris, F-75014, Paris, France
[4]CNRS, UMR7095, Institut d'Astrophysique de Paris, F-75014, Paris, France
[5]Institut d'Astrophysique Spatiale, bat 121, Université Paris Sud 11 & CNRS (UMR8617), 91405 Orsay Cedex, France
[6]Infrared Processing & Analysis Center, California Institute of Technology, 100-22, Pasadena, CA 91125, USA
[7]Center for Astrophysics & Space Sciences, University of California, San Diego, La Jolla, CA 92093-0424, USA
[8]Max-Planck-Institut für Astronomie, 69117 Heidelberg, Germany
[9]Dark Cosmology Centre, Niels Bohr Institute, University of Copenhagen, Juliane Maries Vej 30, DK-2100 Copenhagen Ø, Denmark
[10]California Institute of Technology, 1200 E California Blvd, Pasadena, CA 91125, USA
[11]Institute de Radioastronomie Millimetrique, 200 rue de la Piscine, 380406, St. Martin d'Heres, France
[12]European Southern Observatory, Karl-Schwarzschild Strasse, 85748 Garching bei München, Germany
[13]Department of Physics & Astronomy, University of Sussex, Falmer, Brighton, BN1 9RH, UK
[14]National Radio Astronomy Observatory, P.O. Box 0, Socorro, NM 87801, USA
Received 2009 December 21; Accepted 2010 April 5

ABSTRACT

We present SHARC-2 350 μm data on 20 luminous z$\sim$2 starbursts with $S_{1.2\mathrm{mm}}>2$ mJy from the *Spitzer*-selected samples of Lonsdale et al. 2009 and Fiolet et al. 2009. All the sources were detected, with $S_{350\mu\mathrm{m}}>25$ mJy for 18. With the data we determine precise dust temperatures and luminosities for these galaxies, using on both single-temperature fits and models with powerlaw mass–temperature distributions. We derive appropriate formulae to use when optical depths are non-negligible. Our models provide an excellent fit to the 6 μm–2 mm measurements of local starbursts. We find characteristic single-component temperatures $T_1\simeq35.5\pm2.2$ K and integrated IR luminosities around $10^{12.9\pm0.1}$ $L_\odot$ for the SWIRE-selected sources. Molecular gas masses are estimated at $\simeq4\times10^{10}$ $M_\odot$, assuming $\kappa_{850\mu\mathrm{m}}=0.15$ m^2 kg^{-1} and an SMG-like gas-to-dust mass ratio. The best-fit models imply $\gtrsim$2 kpc emission scales. We also note a tight correlation between rest-frame 1.4 GHz radio and IR luminosities confirming star-formation as the predominant power source. The far-infrared properties of our sample are indistinguishable from the purely submillimeter-selected galaxy (SMG) populations from current surveys. We therefore conclude that our original selection criteria, based on mid-infrared IRAC colors and 24 μm flux densities, provides an effective means for the study of SMGs at z$\sim$1.5–2.5.

Subject headings: galaxies: evolution — galaxies: high-redshift — galaxies: ISM — galaxies: photometry — galaxies: starburst — infrared: galaxies — submillimeter

1. INTRODUCTION

Star-forming galaxies release a significant fraction of their energy output at infrared (IR) and submillimeter wavelengths ($\lambda\sim5$–$1000\,\mu$m in the rest frame). The luminosities of starbursts, with star formation rates over 100 $M_\odot$ yr^{-1}, are almost exclusively carried at infrared wavelengths. Whereas luminous and ultra-luminous infrared galaxies (LIRGs and ULIRGs) are extremely rare in the local Universe, they are prevalent at higher redshifts (e.g. Le Floc'h et al. 2005; Caputi et al. 2007). By studying this population we can learn about the star-formation history of the Universe, and because the starbursting is triggered by merger events, we can also probe models of structure formation and halo dynamics through the ages.

Around 1 mm wavelengths it is possible to find similar starbursts across much of the volume of the Universe, because the dimming of radiation from increasing distances is countered by the steeply rising energy spectrum between 2 mm and 200 μm in the rest frame. Thus, an infrared galaxy would produce nearly the same (sub)mm flux regardless of its distance in the range of z$\sim$0.5–10.

The nearly bias-free selection, together with the fundamental desire for studying starbursts, make submillimeter surveys (Coppin et al. 2006; Weiss et al. 2009; Austermann et al. 2010; Ivison et al. 2010) especially relevant. However, while finding submm galaxies (SMGs) is relatively straightforward, studying them in any detail has proved difficult. This is due to two factors: they are faint at other wavelengths, and there are often multiple possible optical/NIR counterparts (see Pope et al. 2006; Younger et al. 2009) due to the poor spatial resolution of most submm telescopes (typically 10"–30" FWHM).

As a result, most spectroscopic redshifts have been obtained for SMGs with radio-detected counterparts providing the required positional accuracy. Thus, Chapman et al. (2003, 2005) and Kovács et al. (2006) discovered that most SMGs lie around a median redshift of 2.3, are extraordinarily luminous (10^{12}–10^{13} $L_\odot$) and have large molecular gas reservoirs (10^{10}–10^{11} $M_\odot$). The close correlation between IR and radio luminosities of SMGs resembles that of local star-forming galaxies (Helou et al. 1985; Condon & Broderick 1991; Condon 1992; Yun et al. 2001), implying that star-formation is the principal power source.

Despite these successes however, the number of SMGs with spectroscopic redshifts is only around a hundred, and less than half of these are characterized in the far-infrared (FIR).

kovacs@astro.umn.edu

Table 1
Sample Selection Criteria

Band/Instrument	Criterion
IRAC	$S_{3.6\,\mu m} < S_{4.5\,\mu m} < S_{5.8\,\mu m} > S_{8.0\,\mu m}$
MIPS 24	$S_{24\,\mu m} > 400\,\mu$Jy
MAMBO	$S_{1.2mm} \gtrsim 2$ mJy

Note. — Summary of the selection criteria for the MAMBO-detected 5.8 μm-peaker samples of L09 and F09.

Furthermore, the radio-undetected SMG population is almost completely unexplored. A truly unbiased understanding of SMGs requires improved selection methods.

1.1. *SMGs and* Spitzer

A major step forward in understanding SMGs was provided by *Spitzer*. With its sensitive mid-IR imaging and spectroscopic capabilities, *Spitzer* detected most SMGs in multiple mid-IR bands, which can provide accurate photometric redshifts $dz/(1+z)\simeq 0.1$ (Pope et al. 2006, Lonsdale et al. 2009). Furthermore, many *Spitzer*-selected objects are predicted to be submm bright (Lonsdale et al. 2009; hereafter L09). Unfortunately, the identification of mid-infrared counterparts to SMGs is plagued by problems similar to those of optical association (Pope et al. 2006), and so the reliance on radio associations remains.

Selecting strongly luminous starbursts at $z\sim 2$ from *Spitzer* data themselves can overcome these problems, and the resulting samples expected to contain a large proportion of SMGs within them. Thus, a two-step process has been suggested. First, selecting sources with peak *Spitzer*-IRAC flux densities in the 5.8 μm channel should remove galaxies with a mid-IR luminous AGN (Weedman et al. 2006; Farrah et al. 2008), leaving objects with a clear rest-frame 1.6 μm opacity minimum at $z\approx 2$. The required IRAC detections ensure that stellar masses large, esp. when applied to limited sensitivity samples such as SWIRE (Lonsdale et al. 2003). Second, a bright 24 μm flux density cut ($S_{24\,\mu m}>400\,\mu$Jy) favors starbursts at the same redshift as the strong rest-frame 7.7 μm Polycyclic-Aromatic Hydrocarbon (PAH) emission feature is redshifted into the band. Redshifts from IRS spectra or from IRAC photometry confirm that most sources selected in this way lie at $z\simeq 2$ (Weedman et al. 2006, Fiolet et al. in prep). The effectiveness of such a two-pronged selection was confirmed by L09 and Fiolet et al. (2009; hereafter F09), who detected a significant fraction of these sources at 1.2 mm using the MAMBO camera at the IRAM 30-m telescope (i.e. $S_{1.2mm}\gtrsim 2$ mJy). Clearly, the proposed *Spitzer* selection (see Table 1) yields distant luminous starburst galaxies without radio preselection.

A key question is to what extent the SWIRE-selected samples are in fact representative of the purely submillimeter-selected population. A straightforward way to test this is to constrain where the peak of the IR emission lies, thus bridging the gap between the cold dust detected by MAMBO, and the hot dust and PAHs detected by *Spitzer*. Such constraints can be used to derive effective dust temperatures and accurate IR luminosities, for comparison with the overall SMG population. Because the sample consists of galaxies at z$\sim$2, and that dust temperatures are expected in the range of 30–40 K, the 350 μm band offers an ideal opportunity for providing the constraints we seek.

For our study we targeted 12 galaxies from F09 and another 8 from L09. The former is an almost complete sample of sources from 0.5 deg^2 satisfying the criteria of Table 1, whereas the L09 sources are drawn arbitrarily from $\sim$30 deg^2. To enhance our chances of detection at 350 μm, we selected objects with clear MAMBO detections, with an additional preference towards the highest 1.2 mm flux density measurements.

Table 2
Variable Calibrators

Name	Date	N_{obs}	$S_{350\,\mu m}$ (Jy)	Cross Calibrators
CIT6	2007 Jan 17	1	3.14 ± 0.25	Arp 220
	2007 Apr 17	2	3.12 ± 0.11	Arp 220, Vesta
	2008 Jan 18	5	2.21 ± 0.08	Arp 220
	2009 Jan 22–25	16	2.93 ± 0.04	Arp 220, Ceres
3C 273	2007 Apr 19	1	4.08 ± 0.30	CIT6
	2008 Feb 23	2	3.82 ± 0.21	Arp 220
	2008 Feb 24	2	3.84 ± 0.20	Arp 220
	2009 Jan 23	1	5.04 ± 0.37	Arp 220
	2009 Jan 24	3	5.46 ± 0.22	Arp 220, Ceres
	2009 Jan 25	2	5.25 ± 0.25	Arp 220, Ceres

Note. — The columns are: the name of the variable calibrator source, the period of measurements, the number of measurement, the derived 350 μm flux densities, and the stable cross-calibrator sources used.

The observations are described in Section 2 and the results are summarized in Section 3, where we also discuss one of the submm sources, which appears to be a close association of several IR galaxies. In Section 4 we develop appropriate Spectral Energy Distribution (SED) models to interpret the measurements. With these models, we characterize the sample in Section 5, deriving precise dust temperatures, dust/gas masses and luminosities, and with them we verify the (far-)infrared to radio correlation.

We assume a cosmology with H_0=71 km s^{-1} Mpc^{-1}, Ω_M=0.27 and Ω_Λ=0.73, and calculate distances as prescribed by Hogg (1999).

2. SHARC-2 350 μm OBSERVATIONS

350 μm observations were carried out at the 10.4 m Caltech Submillimeter Observatory (CSO), using the SHARC-2 Camera (Dowell et al. 2003). Data were collected during five successful observing runs between January 2007 and February 2009. The typical weather conditions during observing ranged from good to marginally useful, with in-band line-of-sight opacities $\tau\simeq$1–2, corresponding to precipitable water vapor levels around 0.7–1.3 mm.

We took advantage of the open-loop actuated Dish Surface Optimization System (DSOS; Leong et al. 2006) of the telescope to maintain the optimal beam qualities at all elevations. As a result, we expect our telescope beam efficiencies to be relatively high and limited mainly by the 12 μm surface rms of the CSO panels.

Our observing strategy was to modulate the telescope primary with small, field-of-view sized open Lissajous patterns (Kovács 2008b, 2006), with average scanning around a beam per second. These patterns facilitate the separation of the astronomical source from the various correlated signals (of the atmosphere or the instrument). At the same time, the pattern provides uniform coverage over the field-of-view, the source remains exposed on the array at all times, and the scanning mode does not require extreme maneuverability of the telescope structure.

Table 3
Summary of the Far-Infrared and Radio Observations

ID	IAU Name	Offset (arcsec)	z	$S(24\,\mu\mathrm{m})$ (μJy)	$S(350\,\mu\mathrm{m})$ (mJy)	$S(1.2\,\mathrm{mm})$ (mJy)	$S(20\,\mathrm{cm})$ (μJy)	$S(50\,\mathrm{cm})$ (μJy)	$S(90\,\mathrm{cm})$ (μJy)
LH-02	SWIRE_J103639.57+575346.6	+2.2, +1.0	1.93[a]	838 ± 15	54.8 ± 5.8	5.29 ± 0.85	···	···	···
LH-06	SWIRE_J103837.03+582214.7	+3.2, –0.0	1.68[b]	1072 ± 19	45.5 ± 7.1	3.83 ± 0.84	···	···	···
LH-03	SWIRE_J104313.33+574621.0	+1.5, –0.2	2.67[a]	722 ± 17	62.9 ± 10.2	3.79 ± 0.76	···	···	···
L-1	SWIRE_J104351.16+590057.9	+2.7, –1.0	2.26[c]	722 ± 17	34.1 ± 6.7	2.95 ± 0.66	77 ± 9.0	142 ± 19	327 ± 74
L-9	SWIRE_J104440.25+585928.4	+0.6, +0.4	2.01[c]	674 ± 19	57.0 ± 15.1	4.00 ± 0.55	117 ± 9.2	195 ± 22	266 ± 69
L-11	SWIRE_J104556.90+585318.9	+1.3, +0.8	1.95[c]	650 ± 18	39.7 ± 5.9	3.08 ± 0.58	315 ± 4.1	425 ± 43	651 ± 72
L-14	SWIRE_J104638.67+585612.6	+1.6, –0.1	2.07[c]	611 ± 17	31.9 ± 4.9	2.13 ± 0.71	160 ± 6.0	322 ± 33	426 ± 70
L-15	SWIRE_J104656.47+590235.5	+6.3, –0.9	1.89[c]	419 ± 18	26.9 ± 4.2	2.36 ± 0.62	69 ± 3.7	181 ± 21	258 ± 69
L-17	SWIRE_J104704.97+592332.3	–1.2, +0.4	1.99[c]	647 ± 18	39.6 ± 8.5	2.24 ± 0.64	341 ± 33	756 ± 78	1052 ± 75
L-20	SWIRE_J104717.96+590231.8	+4.7, –1.9	2.10[c]	617 ± 19	49.7 ± 6.5	2.66 ± 0.78	51 ± 4.7	166 ± 19	264 ± 72
L-21	SWIRE_J104718.63+584318.1	+0.3, +5.3	1.78[d]	447 ± 16	41.4 ± 7.4	3.09 ± 0.81	138 ± 36	176 ± 39	350 ± 76
L-22	SWIRE_J104720.49+591043.6	+2.5, +1.5	2.57[d]	435 ± 16	18.9 ± 5.7	3.41 ± 0.73	101 ± 7.1	238 ± 26	447 ± 70
L-23	SWIRE_J104726.44+585213.3	+4, –3	2.38[d]	434 ± 17	19 ± 9[e]	3.13 ± 0.86	86 ± 7.2	172 ± 21	242 ± 71
L-25	SWIRE_J104738.32+591010.0	+1.2, –0.3	1.96[c]	723 ± 17	31.8 ± 5.9	2.56 ± 0.74	69 ± 9.0	166 ± 20	348 ± 72
L-27	SWIRE_J104744.59+591413.4	+0.9, –2.4	2.20[c]	523 ± 18	28.7 ± 6.5	2.48 ± 0.73	77 ± 14	106 ± 18	<219
LH-01	SWIRE_J105007.26+571651.0	+1.8, +2.3	1.35[a]	756 ± 12	46.6 ± 7.6	5.65 ± 0.74	···	···	···
EN1-01	SWIRE_J160343.08+551735.8	+2.9, +0.1	2.37[a]	699 ± 14	42.7 ± 8.2	2.81 ± 0.78	···	···	···
EN1-02	SWIRE_J160440.45+533103.0	–0.5, –7.3	1.93[a]	772 ± 18	44.3 ± 9.1	2.46 ± 0.81	···	···	···
EN1-04[f]	SWIRE_J161658.14+535319.3	+0.2, +0.6	2.00[a]	657 ± 15	27.6 ± 10.2	2.82 ± 0.99	···	···	···
EN2-01	SWIRE_J163734.44+415151.4	+0.9, +3.8	1.85[c]	814 ± 20	30.4 ± 5.7	2.52 ± 0.70	···	···	···

Note. — Source IDs prefixed with LH or EN are from L09, whereas those lettered with L are from F09. SHARC-2 detection offsets are with respect to the SWIRE catalog coordinates. 1.2 mm flux densities are from L09 and F09, 20 cm radio data from Owen & Morrison (2008), 50 cm value from Owen et al. (in prep.), while 90 cm points are from (Owen et al. 2009). The quoted rms uncertainties do not include the uncertainties in the calibration.

[a] Photometric redshift from L09.
[b] IRS Spectroscopic redshift from L09.
[c] IRS Spectroscopic redshift from Fiolet et al. (in prep.).
[d] Photometric redshift from F09.
[e] The 350 μm flux density of L-23 is from the undeconvolved image close to the instrument resolution (middle panel of Fig.1).
[f] SWIRE_J161658.14+535319.3 is the only source in our sample with a MIPS 160 μm detection of 81 ± 4 mJy. However, this datum is not included in our fits.

In total, we spent 37.5 hours on the 20 objects observed. We aimed for $5\,\sigma$ detections, or limiting rms noise levels of 10–12 mJy/beam. Pointing and flux density calibration measurements were taken frequently, at least once per hour during the observing period. Our principal flux density calibrators were Mars, Arp 220 (9.93 ± 0.11 Jy, based on our own calibration against planets and asteroids), and the minor planets Ceres, Juno and Vesta, for which appropriate temperature models have been derived by C. D. Dowell and are available through the SHARC-2 web-page[1]. In addition, we relied on the evolved star CIT6, and the quasar 3C 273 as additional calibrators, owing to their relative proximity to the targeted fields in the Lockman Hole. To counter the long-term variability of CIT6 we measured it against our main calibrator sources during each observing run, while 3C 273 we cross-calibrated on a daily basis (see Table 2). Based on the residual scatter of calibrator flux densities, we expect a 350 μm calibration accuracy around 8% for our science targets.

We checked and adjusted the focus settings several times during each night, more frequently near sunrise and sunset when variations tend to be greatest. To avoid the unnecessary smearing of our sources due to systematic pointing errors, the pointing data of each run was carefully analyzed for trends. Corrections were applied as required at the time of reduction. The final pointing accuracy of the SHARC-2 data is expected at $\simeq$3" rms.

We reduced the data using the *CRUSH* software (1.99-a5; Kovács 2008a, 2006), which estimates and removes the correlated atmospheric and instrumental signals, solves for the relative detector gains, and determines the appropriate noise weighting of the time-streams, in an iterated pipeline scheme. To maintain calibration accuracy, the inherent filtering of point source signals by the reduction steps is carefully estimated and corrections are applied internally by *CRUSH*.

[1] `www.submm.caltech.edu/~sharc`

3. RESULTS

We detect all 20 of the targeted sources. In a few cases, the detections are tentative. The measured 350 μm flux densities are listed in Table 3, along with all prior measurements relevant to this work. We reached rms sensitivities of 4–10 mJy/beam in all but one field. 80% of the 350 μm detections are robust ($>4\,\sigma$), 2 are 3–4 σ and another two are marginal ($<3\,\sigma$). However, even the lowest signal-to-noise detection is significant (with a confidence level $>95\%$) given the small, beam-sized search areas surrounding the IRAC (and nearby radio) positions. For the most part, the SHARC-2 positions are in excellent agreement with those from IRAC, with deviations at $\lesssim$3" rms.

3.1. *Submillimeter Multiplets*

There is, however, the curious case of L-23 (see Fig.1), with an elongated $5.7\,\sigma$ SHARC-2 peak 13.5" from the IRAC and radio positions. The discrepancy is too large ($>4\,\sigma$) to be a statistical pointing error. Coincidentally, we have a large number of pointing measurements both before and after observing the galaxy in question, all reinforcing an absolute 350 μm astrometric accuracy better than 3" rms. Thus, the single SHARC-2 peak is inconsistent with a source at the IRAC and radio positions.

A substructure of the peak is revealed if we smooth less than the optimal amount for point source extraction. We find a banana-shaped feature dominating the 350 μm emission to the

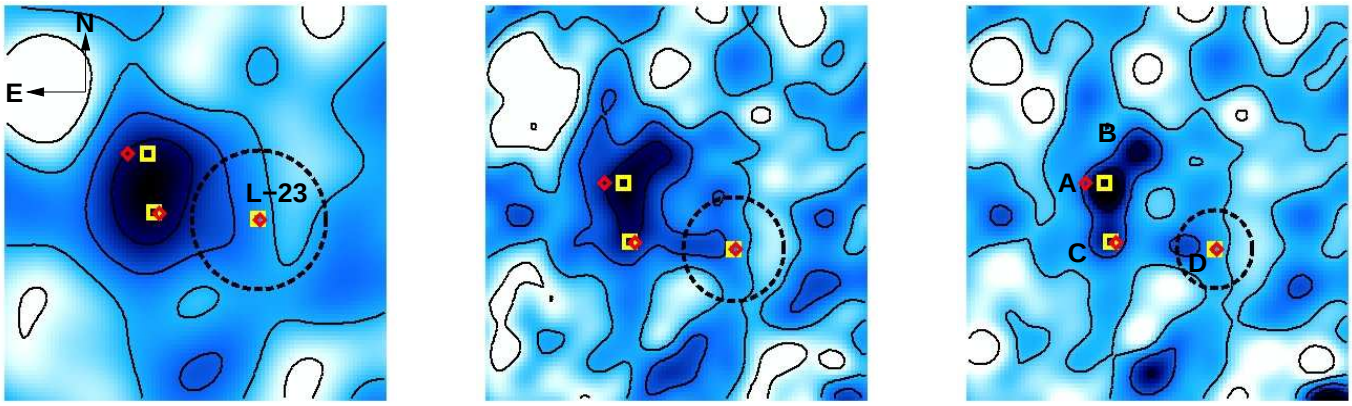

Figure 1. 45”×45” postage stamps around L-23. Left: the beam-smoothed image used for source extraction at ∼11” resolution shows a single peak East of the expected SWIRE source position (dashed circle indicating typical search area). Center: near the diffraction-limited resolution of SHARC-2, the peak resolves into a banana-shaped feature and a hint of a point source close to the IRAC position. The image has been slightly realigned to match the elongated feature with two nearby IRAC galaxies (yellow squares). The nearby radio sources are shown with red diamonds. The search area is reduced as a result of the realignment. Right: a deconvolution suggests up to 4 distinct components (lettered A through D), all within the typical beam areas of current submm surveys. Three of the peaks align well with IRAC sources in the field. Contours are -15, 0, 15, 30, and 45 mJy/beam for the panels on the left and center, and -7.5, 0, 7.5, 15, 22.5 mJy/beam for the image to the right.

Table 4
350 μm Decomposition of L-23

ID	α_{2000}	δ_{2000}	$S_{350\,\mu m}$	Association
A	$10^h47^m28^s.1$	+58°52’20”	25 mJy	IRAC/MIPS24, radio
B	$10^h47^m27^s.6$	+58°52’24”	17 mJy	unknown
C	$10^h47^m28^s.1$	+58°52’15”	14 mJy	IRAC/MIPS24, radio
D	$10^h47^m26^s.9$	+58°52’14”	10 mJy	L-23

Note. — The most likely decomposition of the blended 350 μm emission from the neighborhood of L-23 (F09), ordered in decreasing estimated brightness. The SWIRE/MAMBO source we identify as component D. The uncertainties in the deconvolved flux densities we estimate at around 5 mJy. Positions are estimated to be accurate to $\lesssim$2” rms. The positions of the associated IRAC/MIPS and radio sources are discussed in Sec. 3.1.

East, and a fainter $\simeq 2\,\sigma$ compact peak close to the expected position. The position and point-like nature of the fainter component is consistent with both our pointing accuracy, and the expected size ($\lesssim$1”) of a galaxy at z=2.38. Therefore, we identify this as the 350 μm counterpart to L-23.

Deconvolution of the elongated feature suggests three distinct components. Two of these align well with nearby IRAC and MIPS 24 μm peaks (at $10^h47^m28^s.14$, +58°52’20”.9 and $10^h47^m28^s.04$, +58°52’14”.1) and radio sources (at $10^h47^m28^s.45$, +58°52’20”.9 and $10^h47^m27^s.97$, +58°52’14”.1), while the third peak is perhaps a super-resolution artifact. The positions and approximate brightness of the deconvolved peaks are summarized in Table 4.

It is not unusual to find resolved pairs of submm sources with ∼20”–30” separation (Blain et al. 2004; Greve et al. 2004; Farrah et al. 2006; Weiss et al. 2009). Such pairs are relatively infrequent and correspond to massive dark matter halos ($>10^{13}\,M_\odot$). However, the clustering of SMGs on smaller scales is not well constrained. Therefore, the blending of as many as three or four galaxies into a single 350 μm detection peak (with total $S_{350\,\mu m}\approx$60 mJy) is interesting.

We often assume that each deep-field (sub)mm detection corresponds to just one luminous galaxy, with unique counterparts at optical, infrared, or radio wavelength. Granted, that the clustering of SMGs on scales $\lesssim$15” is not well known, it seems reasonable given the generally low density (∼400/deg^2) of sources in the current, shallow (sub)mm surveys. However, our multiplet puts this assumption to the test: the 350 μm components that we identify around L-23 would constitute a single source under the spatial resolution (15”–30”) of current (sub)millimeter surveys. The fact that it is a triplet or a quadruplet suggests that unresolved doublet, or even triplet (sub)mm sources may abound. The ∼20% fraction of the radio-identified SMGs with multiple radio counterparts (Ivison et al. 2007) could be an indication of the frequency of unresolved (sub)mm multiplets, which is also consistent with Aravena et al. (2010). As such, the ubiquitous presumption that (sub)millimeter sources are individual galaxies may not be entirely justified.

If multiple luminous galaxies are often behind the low-resolution (sub)mm peaks, the implications would be wide ranging. Some or all of the IRAC sources commonly detected close to an uncertain (sub)mm position (e.g. Pope et al. 2006; Younger et al. 2009) could each contribute comparably to the measured (sub)mm flux densities. A commonality of multiplets would imply that (sub)mm source counts may be steeper than what SHADES (Coppin et al. 2006), AzTEC (Austermann et al. 2010), or the LABOCA deep field survey (Weiss et al. 2009) found; by counting multiple faint sources as a single bright one, these surveys would slightly underestimate the abundance of faint galaxies while substantially overestimate the number of bright ones (i.e. ULIRGs and Hyper-LIRGs). Submillimeter surveys by *Herschel* (esp. at 250/500 μm) would be similarly affected. A strong clustering of SMGs at separation angles $\lesssim$20”, i.e. below the smallest scales that current submm surveys can resolve, would be implied. Unresolved multiplets could partially explain why as many as half of the SMGs in literature have no identifiable radio counterparts: as opposed to having one detectable counterpart, there may be a number of associated faint radio sources below the detection level.

4. SPECTRAL ENERGY DISTRIBUTIONS

The addition of the 350 μm data to the existing measurements provides a powerful constraint on the FIR spectral energy distributions (SEDs) of the SWIRE-selected samples of L09 and F09. It allows, for the first time, an accurate characterization of the dust temperatures and luminosities of individual sources in the sample, provided that physically realistic

models of emission are fitted to the observations.

Before the advent of *Spitzer*, reliance on single-temperature dust models for was common practice. Extra temperature components were added as necessary to fit data at wavelengths $\lesssim$100 μm . However, such models were clearly very naïve. Among the many more physically motivated treatments is the pioneering work by Désert, Boulanger & Puget (1990) who considered dusty environments exposed to a range of radiation fields. Their framework has been fine-tuned to better match observations, especially of the aromatic features in the mid-IR (e.g. Dale et al. 2001; Dale & Helou 2002). These models, fitted to well-studied local galaxies, serve as typical templates for interpreting *Spitzer* data.

Our goal is to derive accurate and robust FIR characterizations for our sample of galaxies. In so doing, we wish to move beyond a hodge-podge of temperature components but we also do not need the full complexity of the models with mid-IR detail. Thus, we fitted both single-temperature models (which offer direct comparisons to many previous studies) and power-law temperature distributions for a more accurate description. In the following sections we shall discuss the models and the formulae we use for deriving the essential quantities.

4.1. *Single-Temperature Dust Models*

The simplest model of the thermal IR emission assumes that it can be described as a singular gray-body at a physical temperature T in the rest frame. Such single-T flux densities S_1 are best expressed in terms of the observables: the measurement frequency $\nu_{\rm obs}$, and observed-frame temperature $T_{\rm obs} = T/(1+z)$, as

$$S_1(\nu_{\rm obs}, T_{\rm obs}) = m\, d\Omega\ (1-e^{-\tau})\ B_{\nu_{\rm obs}}(T_{\rm obs}). \qquad (1)$$

The other terms are: the physical solid angle $d\Omega$, the optical depth τ, Planck's black-body law B_ν, and magnification m (for gravitationally lensed objects). The physical solid angle is related to the projected source area A by the angular-size distance D_A as $d\Omega = A/D_A^2$. The optical depth can be estimated as the ratio of the total emitting cross-section of dust particles to the projected area of emission. As such, optical depths must be evaluated in the rest frame of the emission. Adopting a typical power-law frequency dependence for the emissivity for dust particles, optical depths can be expressed in the rest frame of the galaxy as:

$$\tau(\nu_r) = \kappa_0\ \left[\frac{\nu_r}{\nu_0}\right]^\beta \frac{M_d}{d\Omega D_A^2}. \qquad (2)$$

Here, $\nu_r = (1+z)\nu_{\rm obs}$ is the rest-frame frequency, M_d is the total dust mass at an angular-size distance of D_A, κ_0 is the characteristic photon cross-section to mass ratio of particles at frequency ν_0. The spectral emissivity index β can be related to the fractal dimension D of the dust particles as $\beta = D-1$ (Yang 2007). Thus, β values are expected in the range of 1–2, depending on the shape of particles. There have been several attempts for determining appropriate κ values for interstellar dust particles (e.g. Hildebrand 1983; Krügel, Steppe & Chini 1990; Sodroski et al. 1997; James et al. 2002). The resulting scatter of values reflects the difficulty of making such measurements. In this work, we assume $\kappa_{850\,\mu{\rm m}}$=0.15 m^2 kg^{-1}, which matches the value used by Kovács et al. (2006) and is based on an average 125 μm value (Dunne, Eales & Edmunds 2003) assuming β=1.5. As the strength of emission depends on the $\kappa_\nu M_d$ product, the inherent uncertainties in κ ultimately affect the accuracy to which dust masses can be determined. At the same time, the temperatures and luminosities can be determined accurately and independently from the assumptions on the absorption efficiency.

We can calculate single-temperature IR luminosities L_1 by integrating the de-magnified observed flux density at luminosity distance D_L=$D_A(1+z)^2$ from the source:

$$L_1(T) = 4\pi\ D_L^2\ m^{-1} \int_0^\infty S_1(\nu, T)\ d\nu$$

The integration can be performed analytically in the optically thin limit ($\tau \ll 1$), giving

$$L_1(T) = \Gamma(4+\beta)\zeta(4+\beta)\ \frac{8\pi h}{c^2}\ \left[\frac{kT}{h}\right]^4 A_{\rm eff}, \qquad (3)$$

in terms of the effective surface area of emission $A_{\rm eff}$, Planck's constant h, the Boltzmann constant k, the speed of light c, and Riemann's Γ and ζ functions. The same expression is also applicable for the case of optically thick emission ($\tau \gg 1$) by setting β=0. The effective area of emission $A_{\rm eff}$, in the optically thin and thick limits respectively, is given by

$$A_{\rm eff} \approx \begin{cases} M_d \kappa_0 (kT/h\nu_0)^\beta & \text{if } \tau \ll 1 \\ \\ d\Omega D_A^2 & \text{if } \tau \gg 1 \text{ or } \beta \to 0 \end{cases} \qquad (4)$$

Given the relation of the projected surface area to total emitting area (πr^2 vs. $4\pi r^2$ for a sphere), our expression for the optically thick limit recovers the Stefan-Boltzmann law of black-body luminosities. In the optically thin limit, $A_{\rm eff}$ is the physical emitting area at the frequency ν_r=kT/h. From a computational point-of-view, it is practical to approximate the Riemann Γ and ζ functions in Eq. 3 for the range of typical β values:

$$\Gamma(4+\beta)\zeta(4+\beta) \approx 6.45 \exp(1.24\beta + 0.11\beta^2), \qquad (5)$$

which is accurate to about a percent in the range $\beta \simeq$0–2,

Interstellar dust emission is mostly optically thin at FIR wavelengths (λ>100 μm). Only the more extreme galaxies and quasars, or strongly lensed objects, concentrate dust to such an extent that optical depths can become significant over the bulk of the emission spectrum. This is a concern, given the extreme nature of our objects. We therefore would like to also consider the effect of intermediate optical depths in deriving accurate luminosity measures.

4.1.1. *Intermediate Optical Depths*

We can derive approximations for the integrated luminosity for the general case of non-negligible optical depths. Our approach is based on the observation that most of the luminosity is radiated at frequencies close to the gray-body SED peak (see Eq. 1), which is observed near

$$\nu_{\rm pk} \approx (3+\beta)\ \frac{kT_{\rm obs}}{h}. \qquad (6)$$

Around the peak, we can approximate the frequency dependence of the emissivity, i.e. $\epsilon = (1-e^{-\tau})$, with a power law $\epsilon \approx \epsilon_{\rm pk}(\nu/\nu_{\rm pk})^{\beta_{\rm eff}}$, where, by definition, an effective spectral index $\beta_{\rm eff}$ can be calculated as:

$$\beta_{\rm eff} = \frac{\partial \log \epsilon}{\partial \log \nu} = \frac{\nu}{\epsilon}\ \frac{\partial \epsilon}{\partial \nu}. \qquad (7)$$

Table 5
Far-Infrared and Radio Properties of Local Starbursts

Name	D_L (Mpc)	$N_{\rm IR}$	$N_{\rm rad}$	$\lvert\chi_r\rvert$	T_c (K)	γ	$\log M_d$ ($M_\odot$)	$\log L$ ($L_\odot$)	$\tau_{\rm pk}$	q	α
Arp 220	77.6	15	7	0.92	36.4 ± 1.2	7.7(2)	7.92(3)	12.16(2)	0.68	2.47(4)	0.25(4)
IRAS 20551-4250	188	10	1	0.99	37.9 ± 2.4	7.2(3)	7.33(9)	12.09(3)	0.19	2.61(9)	···
IRAS 22491-1808	348	14	1	0.68	39.0 ± 2.0	7.6(3)	7.62(8)	12.20(3)	0.38	2.91(7)	···
M 82	3.57	11	9	0.99	35.4 ± 2.0	7.1(3)	6.12(7)	10.86(2)	0.12	2.39(8)	0.65(5)
NGC 6090	127	11	1	1.81	28.0 ± 1.9	6.9(3)	7.44(8)	11.67(2)	0.15	2.33(12)	···
NGC 6240	105	21	7	1.07	32.3 ± 1.1	7.1(1)	7.56(4)	11.96(2)	0.25	1.84(4)	0.85(3)

Note. — The FIR and radio properties of local starbursts, from the multi-T fits to a selection available IR continuum data in the 6 μm–2 mm range, with β=1.5 and assuming typical emission diameter of 1 kpc (or 300 pc for M 82). The synchrotron component is modeled as a simple powerlaw $S_{\rm rad}\propto\nu^{-\alpha}$. Columns are: the object name, luminosity distance D_L, the number of IR and radio flux density data ($N_{\rm IR}$ and $N_{\rm rad}$) used, the residual scatter $|\chi_r|$ around the fit, the temperature T_c of the dominant cold-component, the mass–temperature index γ, dust masses M_d, integrated IR luminosities L, the optical depth τ around the infrared emission peak $\nu_{\rm peak}$, the radio–(F)IR correlation constant q, and synchrotron spectral index α. Uncertainties are 1 σ total errors. These are indicated in brackets for γ, $\log M_d$, $\log L$, q, and α, and refer to the last digits in the quoted values. Dust masses assume $\kappa(850\,\mu{\rm m})=0.15\,{\rm m^2\,kg^{-1}}$. Plots of these models and the data used for deriving them are available in the online edition.

Substituting the optical depth from Eq. 2 and evaluating at the peak $\tau_{\rm pk}$, we arrive at:

$$\beta_{\rm eff} = \beta\,\frac{\tau_{\rm pk}}{e^{\tau_{\rm pk}}-1}. \tag{8}$$

Thus, the frequency dependence of the emissivity near the peak of the emission can be characterized by an effective gray-body index $\beta_{\rm eff}$. This means that we can rely on Eq. 3 to provide an approximation to the luminosity function, simply by replacing β with $\beta_{\rm eff}$ above together with an effective emission area:

$$A_{\rm eff} \approx \frac{(1-e^{-\tau_{\rm pk}})\;d\Omega\,D_A^2}{(3+\beta)^{\beta_{\rm eff}}}. \tag{9}$$

It is possible to refine this approximation by seeking simultaneous solutions to Eqs. 6 and 8 with $\beta\rightarrow\beta_{\rm eff}$ in Eqs. 6 and 9.

4.2. *Power-Law Temperature Distributions*

Single-temperature models can be useful, especially for offering comparison to earlier studies that analyzed data in this way. However, it is clear that such models fall short on the Wien side of the thermal emission spectrum (dotted line on left panel of Fig. 2). Measurements at wavelengths shorter than the peak (typically $\simeq$200 μm) by *IRAS*, *ISO* or *Spitzer* all indicate that flux densities fall far less dramatically than single-T gray-body models imply. Temperature estimates are biased by the inclusion of data on the Wien side (at $\lesssim$200 μm in the rest frame), and luminosities are systematically underestimated. The errors can be significant depending on the actual spectral profile, and the data used for fitting. This is a concern, since the SHARC-2 350 μm point translates to rest frame wavelengths of 90-175 μm at redshifts z$\sim$1–3.

For improving our models, we look for clues in the same local starbursts that yield the oft-used templates for the interpretation of *Spitzer* data (Berta 2005; Polletta et al. 2007). Based on these galaxies we find that a powerlaw distribution of temperature components ($dM_d/dT\propto T^{-\gamma}$), with a low-temperature cutoff at T_c are in excellent agreement with measurements (Fig. 2). At the same time, powerlaw distributions are easily justified in a physical context. The radiative-transfer models of Dale et al. (2001) and Dale & Helou (2002) are similarly conditioned on dust being distributed in a range of radiation fields U as $dM/dU\propto U^{-\alpha}$. Their powerlaw index α is also the Wien-side spectral index and depends on the geometric configuration of dust clouds relative to the heating sources. Under the assumption of radiative dust heating the two models are approximately equivalent with $\gamma\approx4+\alpha+\beta_{\rm eff}$. Therefore, we expect $\gamma\approx$6.5–7.5 for sources embedded in a diffuse medium (e.g. star-formation), and $\gamma\approx$4–5 if absorption happens inside a dense medium at a well-defined distance from the source (e.g. for a molecular ring surrounding an AGN).

We argue that a temperature distribution (as opposed to a radiation-field distribution) offers a more general treatment, because it can also account for non-radiative heating of dust particles, e.g. by shocks or gravitational collapse. One needs only to remember that one of the critical functions of dust in star-formation is to act as a coolant during the collapse of star-forming gas clouds. Thus, dust heating begins even before the UV-bright OB stars illuminate the interstellar medium. Temperature distributions can further arise from a distribution of individual molecular clouds in a galaxy, each with its own size and environment.

Apart from the physical plausibility of power-laws, a practical advantage is that they add just a single variable γ to the parametrization of single-T models. This is welcome, especially since the number of SED measurements across the FIR band are generally few, even for many well-studied local galaxies, allowing robust constraining only for a handful of parameters.

We can write appropriate expressions for predicted flux densities in terms of the single-T flux S_1 (Eq. 1) as

$$S_{\nu_{\rm obs}}(T_c) = (\gamma-1)\;T_c^{\gamma-1}\int_{T_c}^{\infty} S_1(\nu_{\rm obs},T_{\rm obs})\;T^{-\gamma}\;dT, \tag{10}$$

where once again $T_{\rm obs}=T/(1+z)$. The integration can be performed numerically with a number of discrete temperature components, or can be written in a closed form (see Kölbig 1970) using the incomplete Riemann zeta function $Z_1(\gamma-1,\;h\nu_r/kT_c)$ and $\Gamma(\gamma-1)$. Luminosities can be expressed in a closed form and are given by

$$L = \frac{\gamma-1}{\gamma-(5+\beta_{\rm eff})}\,L_1(T_c), \tag{11}$$

based on the single-T value L_1 (Eq. 3). Finiteness of luminosities requires that γ be larger than 5+$\beta_{\rm eff}$.

Our measure of the luminosity accounts for the full power radiated through thermal dust emission, in contrast to a more traditionally defined FIR or IR luminosities, which measure output inside a strictly defined wavelength ranges (e.g. be-

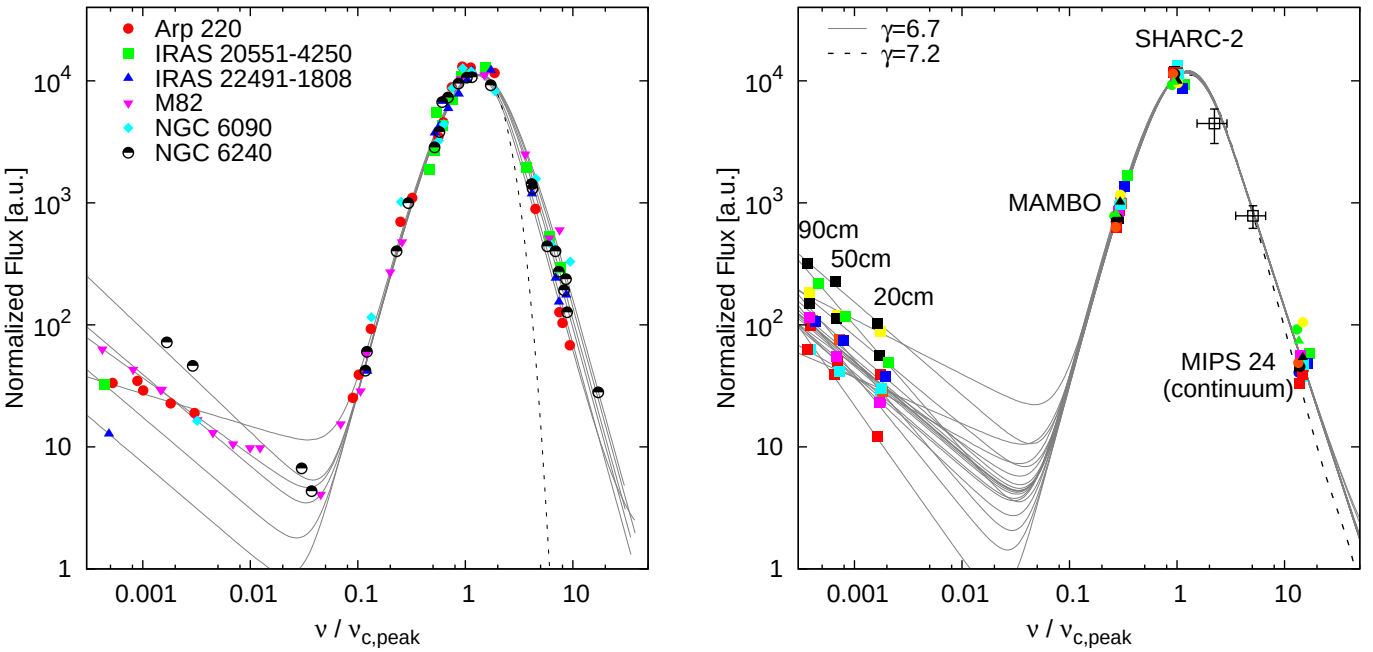

Figure 2. Composite radio and IR continuum SEDs of local starbursts (left) and the SWIRE/MAMBO sample (right). The gray lines represent the best-fit gray-body models with powerlaw mass–temperature distributions using γ=7.2 for the local starbursts and γ=6.7 for the SWIRE-selected sample. Frequencies are normalized to the peak of the cold-component emission (Eq. 6). A single-T model is shown on the left panel for comparison (dashed line), demonstrating the shortcoming of such models on the Wien side. The continuum contribution to the 24 μm flux density is estimated based on the average IRS spectra of eight L09 galaxies. The average local starburst model with γ=7.2 is also shown on the right panel for comparison (dashed line). We also show the stacked average 70 μm and 160 μm flux densities of F09 sources (black hollow squares with error bars) for a fictive source with median properties (T_c=33.5 K, M_d=7×10^8 M$_\odot$ at z=2.05). Individual SED plots are available in the online edition.

tween 40 μm and 1000 μm). As such, our expression for the integrated luminosity can be applied to a wider range of environments (e.g. hot accretion disks) than definitions based on strict wavelength ranges. Additionally, L provides a fair proxy for the total bolometric luminosity of warm ($\gtrsim$30 K) luminous infrared galaxies (LIRGs), where an overwhelming fraction of the total power output is absorbed and re-radiated by dust.

4.2.1. *Clues from Local Starbursts*

To check what β and γ describe the local starbursts best, we fitted a selection[2] of published FIR continuum data uncontaminated by aromatic features or synchrotron emission, in the 6 μm–2 mm range, with power-law T-distributions and assuming kpc-scale emission. For M 82 we have assumed a characteristic emission diameter of 300 pc, in line with the observed size of its molecular ring. Our fitting routine performs a generic χ^2 minimization based on the downhill simplex method described by Press, Flannery & Teukolsky (1986). The results are summarized in Table 5.

Encouraged by the consistent γ values within measurement error, we stipulate that the temperature distribution is possibly sufficiently universal for star-forming galaxies, so that we may proceed to fit γ and β globally, while keeping T_c and M_d as individual parameters for each galaxy. We do this by nesting an inner χ^2 minimization loop for T_c and M_d for each objects, in an external fitting of β and γ for all. Thus we find that $\beta = 1.53 \pm 0.04$ and $\gamma = 7.22 \pm 0.09$ describe the local starburst best, producing close to the expected level of residual scatter based on the measurement and calibration uncertainties. The resulting β is in excellent agreement with measurements both in the Galaxy (Dupac et al. 2003) and in the laboratory (Agladze et al. 1996). Under the assumption of radiative dust heating, the values of γ and the characteristic opacities $\tau \gtrsim 0.3$ on the Wien side imply radiation-field index $\alpha \gtrsim 2.35$, in good agreement with the predicted value of 2.5 for sources embedded in a diffuse medium (Dale et al. 2001). The conclusions on β and γ hold for a wide range of possible emission scales around the assumed values.

[2] We relied on the on-line NASA Extragalactic Database (NED) for flux densities. When more than one measurement was available for a given band we generally opted for the most recent one, or the one with the lowest measurement uncertainty. Additionally, we supplemented the data for M 82 in the 350 μm–2 mm range with Leeuw & Robson (2009) and Alton et al. (1999). For Arp 220, we also included our own 350 μm measurement of 9.83±0.11 Jy in the analysis.

4.3. *Sample Characterization*

In characterizing our SWIRE-selected samples, we assume β=1.5 based on our findings on local starbursts and work by others. For the size of the emitting region (i.e. for setting $d\Omega_A D_A^2$) we assume an average diameter of 3 kpc in our single-temperature fits. Such an extended starburst is unprecedented in the local universe, where the luminosities tend to originate from smaller kpc-scale molecular rings. Nevertheless, the larger sizes are reasonable for our sample (see e.g. Farrah et al. 2008), where luminosities exceed the local examples by one-or-two orders of magnitude. The assumption on the extent of emission is critical only for interpreting the temperature parameter of the fit as a true measure of physical temperatures. The best-fit temperature values would rise if smaller emission diameters were assumed. At the same time, dust masses and integrated luminosities remain nearly independent of the size assumption, and thus offer robust characterizations. The resulting single-temperature fits to the sample are summarized in Table 6.

The FIR properties derived from the single-T fits are based on the MAMBO 1.2 mm measurement and our SHARC-

2 350 μm data only. Shorter wavelength data (esp. MIPS 24 μm) were not included in these fits because these trace higher-temperature components and aromatic features, neither of which are accounted for in the single-T dust model. We also do not include the 160 μm datum of EN1-04 for any in our modeling, because we find it inconsistent with the other measurements. We suspect that the uniquely detected 160 μm flux density of our sample may be contaminated by an unknown source close to EN1-04.

Even with all the caution we can summon, single-temperature models cannot yield accurate characterizations for reasons already disserted. We include these simple models only to provide a comparison to other studies (esp. Kovács et al. 2006), which analyze FIR and submm data in this way. Fitting a distribution of dust temperatures to the data yields more realistic estimates of the dust masses and luminosities. Our best estimates of the underlying FIR properties are summarized in Table 7, and shown on Fig. 2. The temperature parameter T_c indicates the temperatures of the dominant coldest component, above which warmer components exist in lesser quantities (see Sec. 4.2). Therefore, it is not surprising that single-component fits, which measure an average temperature, should yield characteristic values above the cold cutoff temperatures T_c in a distribution.

For our temperature-distribution fits we have included the MIPS 24 μm data as guiding constraints on the short-wavelength tails of the dust continuum. It is clear, however, that the 24 μm flux density is likely dominated by emission from aromatic features. However, warm dust and PAH likely cohabit the same interstellar environments. Thus, PAH emission is almost certainly coupled to a comparably bright dust continuum. Consequently, one should anticipate close to constant PAH-to-continuum flux ratios for a class of star-formation dominated objects. Based on the stacked IRS spectra of L09 we can estimate the typical continuum contribution to the MIPS 24 μm measurement as a function of redshift (Fig. 3), with which we set appropriate 24 μm constraints for our fits. Recognizing, however that the continuum fraction may vary significantly from one galaxy to the next, we assign an uncertainty of 0.25 dex to these 24 μm guesstimates. Thus we allow the 24 μm continuum fraction to span a full decade in brightness before the deviation becomes significant (i.e. $>2\,\sigma$), while we assume that the average IRS spectrum of L09 is representative of the sample as a whole.

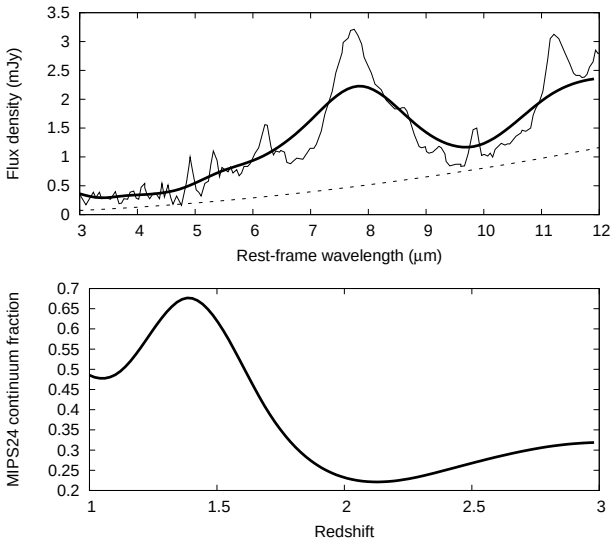

Figure 3. Expected continuum contribution to the MIPS 24 μm measurements. The top panel shows the average IRS spectra of eight L09 sources (thin solid line), and as it would appear under the resolution of the MIPS 24 μm band (thick solid curve). Based on the decomposition of this spectrum into starburst PAH features (NGC3079) and a power-law continuum (dashed line) contribution $\sim\lambda^2$ (see L09), we estimate the typical continuum contributions to the MIPS 24 μm flux as a function of redshift (bottom panel) for the SWIRE-selected samples of L09 and F09, which we use to derive appropriate continuum constraints at 24 μm for our SED fits.

5. DISCUSSION

Under the assumption of extended starbursts we find that our models deviate from the optically thin limit only moderately, with $\tau\approx0.7\pm0.2$ near the emission peaks (under the assumed emission diameters of 3 kpc). This is good news for a straightforward comparison to the SMGs of Kovács et al. (2006), which was analyzed under the optically thin assumption. These optical depths are not much higher than the opacities of local starbursts on kpc scales. We may take this as a first indication that our guess on the extent of star-formation is correct.

The median 70 μm and 160 μm flux densities of 2.56 ± 0.38 mJy and 14.63 ± 4.05 mJy respectively from the stacked images of the MAMBO-detected sources of F09 agree well with the multi-T models of our sources with median properties (i.e. T_c=33.5 K, M_d=$10^{8.82}$ M$_\odot$ at z=2.05), within the expected measurement uncertainties (see Fig. 2). These prove the general reliability of the 24 μm continuum contribution estimates.

The use of the scaled 24 μm data further allows us to probe the range of γ values and typical emission scales that are consistent with measurements. Accordingly, we find $\gamma=6.71\pm0.11$ and average emission diameters around $\simeq$2 kpc fit the data best globally. We can exclude diameters $<$1.2 kpc with 95% confidence. Thus, we see our size assumption for the single-T fits sufficiently justified. At the same time, we adopt the most likely diameter of 2 kpc in our multi-T fits.

The result on the sizes is significant because it provides an indirect measure of the true extent of the FIR emission in hyper-luminous infrared galaxies (HLIRGs). Interferometric imaging by Tacconi et al. (2006) already hinted at similar scales based on slightly broadened CO emission profiles (vs. their synthesized beams). The broadening however can also result from distinct compact nuclei separated at the inferred distance (e.g. in a merging system), whereas the best-fit SEDs are only consistent with extended dust emission. The implied scales, spanning kilo-parsecs across, are in line with Farrah et al. (2008) and are a strong indication that dust heating is distributed, which in turn supports star-formation as the primary power source.

For star-forming galaxies we expect $\gamma\approx6.5+\beta_{\rm eff}$ based on (Dale et al. 2001). With $\tau_{\rm pk}\gtrsim1.2\pm0.4$ near the emission peaks (corresponding to the most likely emission diameters of 2 kpc), it is not surprizing that the SWIRE-selected sample has γ values below those of local starbursts. The relatively shallow temperature distributions in turn might explain the unusually high 24 μm to 1.2 mm flux density ratios reported by L09 and F09. The implied radiation-field distribution indeces $\alpha\gtrsim$2.0–2.35 further support star-formation as the primary heating source behind the extreme luminosities.

The average dust mass in our sample is 7×10^8 M$_\odot$. All of our galaxies have masses near the mean value, within the typical 40% (i.e. 0.15 dex) measurement error, revealing only a hint of an underlying scatter $\lesssim$20%. Assuming SMG-

Table 6
Single-Temperature Characterizations

ID	T (K)	$\log M_d$ ($M_\odot$)	$\log L_1$ ($L_\odot$)	q
LH-02	36.5 ± 2.7	9.13 ± 0.15	12.66 ± 0.10	···
LH-06	33.7 ± 3.7	9.03 ± 0.19	12.46 ± 0.15	···
LH-03	53.5 ± 7.7	8.66 ± 0.20	13.23 ± 0.21	···
L-1	39.1 ± 4.9	8.79 ± 0.20	12.64 ± 0.17	2.16 ± 0.18
L-9	41.3 ± 6.4	8.90 ± 0.17	12.82 ± 0.24	2.41 ± 0.25
L-11	37.5 ± 4.3	8.85 ± 0.18	12.59 ± 0.15	1.83 ± 0.16
L-14	40.4 ± 7.3	8.63 ± 0.28	12.61 ± 0.22	1.94 ± 0.22
L-15	33.9 ± 4.3	8.81 ± 0.22	12.34 ± 0.15	1.99 ± 0.16
L-17	43.3 ± 8.9	8.61 ± 0.26	12.75 ± 0.29	1.76 ± 0.29
L-20	46.9 ± 8.8	8.63 ± 0.26	12.93 ± 0.25	2.48 ± 0.26
L-21	36.0 ± 5.1	8.89 ± 0.22	12.52 ± 0.19	2.17 ± 0.20
L-22	33.4 ± 3.5	8.97 ± 0.18	12.41 ± 0.15	1.56 ± 0.16
L-23	32.8 ± 5.7	8.95 ± 0.24	12.36 ± 0.26	1.80 ± 0.27
L-25	36.3 ± 5.3	8.79 ± 0.22	12.48 ± 0.18	2.07 ± 0.19
L-27	36.3 ± 5.6	8.77 ± 0.25	12.47 ± 0.20	2.30 ± 0.21
LH-01	27.1 ± 2.0	9.35 ± 0.13	12.16 ± 0.11	···
EN1-01	45.6 ± 7.7	8.66 ± 0.24	12.89 ± 0.23	···
EN1-02	43.2 ± 9.4	8.65 ± 0.29	12.77 ± 0.30	···
EN1-04	33.6 ± 6.2	8.89 ± 0.28	12.38 ± 0.26	···
EN2-01	34.5 ± 4.9	8.82 ± 0.23	12.39 ± 0.18	···

Note. — All quantities were fitted using a single-temperature model with β = 1.5 and assuming a 3 kpc emission diameter. The dust masses assume $\kappa(850\,\mu\mathrm{m})$=0.15 $\mathrm{m^2\,kg^{-1}}$. Uncertainties are 1 σ total errors of the fits to data, which do not include the uncertainties in the redshift values.

Table 7
Realistic Characterizations

ID	T_c (K)	$\log M_d$ ($M_\odot$)	$\log L$ ($L_\odot$)	q
LH-02	34.6 ± 1.9	9.07 ± 0.13	12.97 ± 0.08	···
LH-06	33.5 ± 2.9	8.86 ± 0.18	12.93 ± 0.12	···
LH-03	45.0 ± 3.4	8.71 ± 0.12	13.44 ± 0.13	···
L-1	35.6 ± 2.8	8.73 ± 0.16	13.04 ± 0.12	2.25 ± 0.15
L-9	34.8 ± 3.0	8.93 ± 0.12	12.99 ± 0.15	2.28 ± 0.16
L-11	33.2 ± 2.4	8.84 ± 0.13	12.91 ± 0.11	1.85 ± 0.13
L-14	33.5 ± 2.7	8.69 ± 0.16	12.93 ± 0.12	1.97 ± 0.15
L-15	29.8 ± 2.3	8.78 ± 0.16	12.73 ± 0.11	2.08 ± 0.14
L-17	34.1 ± 2.9	8.71 ± 0.14	12.96 ± 0.14	1.67 ± 0.16
L-20	36.7 ± 2.7	8.77 ± 0.13	13.09 ± 0.11	2.34 ± 0.14
L-21	31.1 ± 2.4	8.91 ± 0.15	12.80 ± 0.12	2.15 ± 0.15
L-22	33.1 ± 2.7	8.79 ± 0.21	12.91 ± 0.11	1.76 ± 0.15
L-23	33.0 ± 2.7	8.78 ± 0.21	12.90 ± 0.14	2.04 ± 0.17
L-25	32.7 ± 2.7	8.74 ± 0.17	12.89 ± 0.13	2.17 ± 0.16
L-27	31.9 ± 2.7	8.75 ± 0.17	12.84 ± 0.13	2.38 ± 0.16
LH-01	27.7 ± 1.7	9.21 ± 0.15	12.58 ± 0.09	···
EN1-01	38.5 ± 3.1	8.70 ± 0.15	13.17 ± 0.13	···
EN1-02	34.7 ± 3.0	8.75 ± 0.15	12.99 ± 0.14	···
EN1-04	32.0 ± 3.0	8.77 ± 0.22	12.85 ± 0.15	···
EN2-01	32.5 ± 2.9	8.70 ± 0.18	12.88 ± 0.13	···

Note. — Same as Table 6, except that properties are derived for a power-law temperature-distribution with γ = 6.7, and a most-likely value of 2 kpc is assumed for the emission diameter. We used $\kappa(850\,\mu\mathrm{m})$=0.15 $\mathrm{m^2\,kg^{-1}}$, and β=1.5 in deriving the quantities.

like gas-to-dust mass ratios of 54 (Kovács et al. 2006), which are also typical to the nuclear regions of nearby galaxies (Seaquist et al. 2004), we estimate an average molecular gas content for our sample in the neighbourhood of $4\times10^{10}\,\mathrm{M_\odot}$.

Our analysis reveals no statistical difference between the L09 and F09 subsamples. Table 8 offers a comparison of average properties between the subsamples, the combined SWIRE/MAMBO sources and the classical SMGs. The results from the single-T fits are statistically indistinguishable from the values found for classical SMGs by Kovács et al. (2006). As such, we tentatively conclude that their samples consists predominantly of classical SMGs, although with a more restricted range of redshifts ($z\simeq2.05\pm0.30$) than the purely submillimeter-selected samples. The narrow redshift distribution is a direct product of our selection critera, which favor objects close to $z\approx2$. Since the radio co-selected SMG population peaks around $z\approx2.3$ (Chapman et al. 2003, 2005), we conclude that two-pronged SWIRE-selection (seeking the 24 μm-bright population of 5.8 μm peakers) is effective in identifying a representative subset of SMGs at mid-infrared wavelengths.

5.1. *Radio-FIR Correlation*

Our dust fits point to a tight correlation between IR and radio luminosities. This is witnessed by the consistent q values in Tables 6 and 7, which were calculated according to Eq. 12. Such correlations are well known for various local galaxies (e.g. Helou et al. 1988; Condon & Broderick 1991; Condon 1992; Yun et al. 2001), and extend to various populations into the distant universe (see Garrett 2002; Appleton et al. 2004; Beelen et al. 2006; Kovács et al. 2006). A flux density-based measure of the correlation was originally formulated by Helou et al. (1985) using 1.4 GHz radio and *IRAS* 60 μm and 100 μm flux densities. However, since we do not have the data in the rest-frame *IRAS* bands to use with the original definition, we can either guess these from our models, or re-define the correlation in terms of the quantities we can measure more directly.

The existence of the correlation is not surprising as both the synchrotron emission and the infrared luminosities are driven by the short-lived population of high mass ($>8\,\mathrm{M_\odot}$) stars. The synchrotron emission arises when relativistic electrons, which are produced by supernovae, decelerate in the magnetic fields of galaxies. At the same, the IR heating is dominated by the luminosities of massive OB stars. With short-lived massive stars responsible for both, measures based on luminosities, not flux densities, are expected to capture the essence of the correlation more accurately. Unlike many prior studies of the correlation, we have the advantage of well-constrained, precise luminosity estimates. Accordingly, we can express the logarithmic correlation constant as

$$q = \log\left(\frac{L}{\nu_n\,\mathcal{L}_{1.4\,\mathrm{GHz}}}\right), \tag{12}$$

with an appropriately chosen normalization frequency ν_n for the IR luminosity. The rest-frame radio luminosity density $\mathcal{L}_{1.4\,\mathrm{GHz}}$ is calculated from the observed flux density $S_{1.4\,\mathrm{GHz}}$ using:

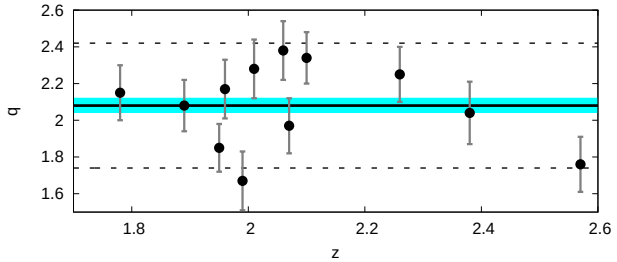

Figure 4. The radio to (far-)infrared correlation. We plot the q values for our sample, computed according to Eq. 12 using the luminosities from Table 7 and ν_n=9 THz. Also shown are the best fit ensemble average value of 2.08 ± 0.04 (solid line with shaded band), and the estimated 2 σ underlying scatter of data around it (dotted lines).

Table 8
Comparison to Classical SMGs

Sample	T_1 (K)	T_c (K)	$\log M_1$ ($M_\odot$)	$\log M_d$ ($M_\odot$)	$\log L_1$ ($L_\odot$)	$\log L$ ($L_\odot$)	q	$\tau_{\rm pk}$	γ
local starbursts[a]	···	34.7 ± 3.6	···	7.33 ± 0.62	···	11.82 ± 0.51	2.42 ± 0.35	0.3 ± 0.2	7.22 ± 0.09
L09	36.1 ± 5.8	34.4 ± 4.2	8.96 ± 0.18	8.85 ± 0.12	12.59 ± 0.28	12.97 ± 0.22	···	1.4 ± 0.5	···
F09	36.5	33.1	8.83	8.80	12.54	12.91	2.08 ± 0.16	1.1 ± 0.2	···
L09 + F09	35.5 ± 2.2	33.5 ± 2.1	8.90 ± 0.07	8.82	12.56 ± 0.05	12.93 ± 0.12	···	1.2 ± 0.4	6.71 ± 0.11
SMGs	34.1 ± 9.5	$(30.4\pm8.5)^b$	8.96 ± 0.32	$(8.85\pm0.18)^b$	12.60 ± 0.48	$(12.76\pm0.61)^b$	2.12 ± 0.12	$(1.2\pm0.5)^b$	···
SMGs ($1.5<z<2.5$)	32.1 ± 5.6	$(30.8\pm5.5)^b$	9.07 ± 0.26	$(8.87\pm0.11)^b$	12.57 ± 0.30	$(12.82\pm0.35)^b$	2.05 ± 0.21	$(1.2\pm0.4)^b$	···

Note. — A comparison of our *Spitzer*-selected samples to the local starbusts, and the classical SMGs of Kovács et al. (2006). Indicated are the ensemble average values and $1\,\sigma$ intrinsic scatters for: characteristic dust temperature (i.e. single-T temperature) T_1, cold-component temperature T_c, single-T dust mass M_1, dust mass M_d, single-T luminosity L_1, total (IR) luminosity L, the (F)IR–radio correlation measure q, and the characteristic opacity $\tau_{\rm pk}$ near the peak of the emission. Only mean values are shown, when the instrisinc scatters are not detected. The last column shows the average mass–temperature distribution index γ and its rms uncertainty. The dust masses assume $\kappa(850\,\mu{\rm m})=0.15\,{\rm m}^2\,{\rm kg}^{-1}$.

[a] These are the local starbursts of Table 5, which provide the SWIRE starburst templates (Berta 2005; Polletta et al. 2007).

[b] Based on our own multi-T fits to the Kovács et al. (2006) data and assuming γ=6.7.

$$\mathcal{L}_{1.4\,\rm GHz} = 4\pi D_L^2\,(1+z)^{1-\alpha}\,S_{1.4\,\rm GHz} \qquad (13)$$

in terms of the luminosity distance D_L, and radio spectral index α. The analysis of the SWIRE/MAMBO sample uses α values quoted in F09, while for the local starbursts we fitted α along with the other parameters.

It is practical to choose the normalization frequency ν_n such that the resulting q values can be compared directly to the widely used original measure of Helou et al. (1985), which assumed typical temperatures of 40 K. We pick ν_n such that the definitions match exactly at that temperature, giving $\nu_n\rightarrow4.52\,$THz used with L_1 (see Kovács et al. 2006), or $\nu_n\rightarrow9.0\,$THz used with L assuming γ=7.2. Consequently, our q values closely mimic the Helou et al. (1985) definition. The correlation measures q for our single- and multi-temperature fits are listed in Tables 6 and 7 respectively.

A different definition was suggested recently by Ivison et al. (2010), who normalize IR-luminosities, measured in the 8–1000 μm band, with ν_n=3.75 THz intended for the 40–120 μm band by Helou et al. (1985). Their measure no longer offers a direct comparison to many earlier studies, which is why we prefer ours. However, our q values can be compared to Ivison et al. (2010) after adding 0.38 (i.e. $\log[9.0/3.75]$).

We find best-fit average q values of 2.11 ± 0.08 with the single-temperature dust models and 2.08 ± 0.04 for the power-law temperature distributions. The implied intrinsic scatters, over the measurement uncertainties, are estimated at 0.18 and 0.16 respectively. Both our mean values and intrinsic scatters (Fig. 4) are significantly below those in local studies, and comparable to the SMGs analyzed by Kovács et al. (2006), and to the $q_{\rm IR}\sim2.40$ found by Ivison et al. (2010) for their correlation measure. The result further supports the conclusion that our sample primarily consists of classical SMGs, without significant excess heating either by an AGN, or by low-mass stellar populations (which are likely partially responsible for the higher average q values observed in the local Universe).

6. CONCLUSIONS

Our main conclusion is that the mid-IR selection criteria of the L09 and F09, picking the bright 24 μm sources that are also 5.8 μm peakers, is effective in identifying a significant fraction of the SMG population around $z\simeq2$, thus providing a means of enhancing our understanding of the elusive submillimeter-selected galaxy population through studies at mid-infrared and shorter wavelengths. The FIR characteristics (dust masses, temperatures and infrared luminosities) of the SWIRE-selected sources are essentially identical to those of the classical SMGs at the same redshift. Additionally, the SWIRE-selected sample exhibits a correlation between radio and IR luminosities that is indistinguishable from that seen for SMGs. Our other conclusions are:

- To provide realistic FIR characterizations for the sample, we developed new models for the spectral energy distributions (SEDs) of galaxies with power-law mass distributions of temperature components. We demonstrated that such models describe local starbursts extremely well, under a tightly constrained dust emissivity index $\beta\simeq1.5$ and mass-temperature index $\gamma\simeq7.2$. The γ values are consistent with what we expect for heating dominated by star-formation.
- We find that the most likely infrared spectral continuum shapes of the distant SWIRE-selected starbursts differ only slightly from the local examples, with best-fit $\gamma\simeq6.7\pm0.1$. The lower γ values are consistent with star-formation under the high optical depths ($\tau_{\rm pk}\simeq1.2$) in our sample.
- Relying on the stacked IRS spectra of L09 for estimating the 24 μm continuum contribution, we place the typical diameter of starburst activity in these SMGs above 1.2 kpc (with 95% confidence), and find a most likely value of 2 kpc.
- The emission scales, the typical γ, and the consistently low q values all confirm that star-formation is the main power source in the galaxies of the sample.
- One of our targets, shows a close clustering of three or four 350 μm components, each of which contributes comparably to the observable 350 μm flux density under the 15”–30” resolution of most current submm surveys. A commonality of unresolved SMG multiplets could bias our understanding of this population. We need further studies to explore the importance of close multiplets in current and future submillimeter surveys.

The authors are extremely grateful to Tom Phillips for contributing extra observing time when we needed it most.

The CSO is funded by the NSF Cooperative Agreement AST-083826.

Facilities: CSO (SHARC-2)

REFERENCES

Agladze, N. I., Sievers, A. J., Jones, S. A., Burlitch, J. M., & Beckwith, S. V. W. 1996, ApJ, 462, 1026
Alton, P. B., Davies, J. I., & Bianchi, S. 1999, A&A, 343, 51
Appleton, P. N., et al. 2004, ApJS, 154, 147
Aravena, M., et al. 2010, ApJ, 708, 36
Austermann, J. E., et al. 2009, MNRAS, 401, 160
Beelen, A., et al. 2006, ApJ, 642, 694
Berta, S. 2005, PhD thesis, Padua University, Italy
Berta, S., Lonsdale, C. J., & Siana, B. 2007, A&A, 467, 565
Blain, A. W., Chapman, S. C., Smail, I., & Ivison, R. 2004, ApJ, 611, 725
Caputi, K. I., et al. 2007, ApJ, 660, 97
Chapman, S. C., Blain, A. W., Ivison, R. J., & Smail, I. 2003, Nature, 422, 695 (C03)
Chapman, S. C., Blain, A. W., Smail, I., & Ivison, R. J. 2005, ApJ, 622, 772
Condon, J. J., & Broderick, J. J. 1991, AJ, 102, 1663
Condon, J. J. 1992, ARA&A, 30, 575
Coppin, K., et al. 2006, MNRAS, 372, 1621
Dale, D. A., Helou, G., Contursi, A., Silbermann, N. A., & Kolhatkar, S. 2001, ApJ549, 215
Dale, D. A., & Helou, G. H. 2002, ApJ, 576, 159
Désert, F.-X., Boulanger, F., & Pouget, J. L. 1990, A&A, 237, 215
Dowell, C. D., et al. 2003, Proc. SPIE, 4855, 73
Dunne, L., Eales, S. A., & Edmunds, M. G. 2003, MNRAS, 341, 589
Dupac, X., et al. 2003, A&A, 404, L1
Farrah, D., et al. 2006, ApJ, 641, 17
Farrah, D., et al. 2008, ApJ, 677, 957
Fiolet, N., et al. 2009, A&A, 508, 117
Garrett, M. A. 2002, A&A, 384, L19
Greve, T. R, Ivison, R. J., Bertoldi, F., Stevens, J. A., Dunlop, J. S., Lutz, D., & Carilli, C. L. 2004, MNRAS, 354, 779
Helou, G., Soifer, T., & Rowan-Robinson, M. 1985, ApJ, 298, L7
Helou, G., Khan, I. R., Malek, L., & Boehmer, L. 1988, ApJS, 68, 151
Hildebrand, R. H. 1983, QJRAS, 24, 267
Hogg, D. W. 1999, arXiv:astro-ph/9905116
Hopkins, A. M. 2007, PASPC, 380, 423
Ivison, R. J., et al. 2007, MNRAS, 380, 199
Ivison, R. J., et al. 2010, MNRAS, 402, 245
James, A., Dunne, L., Eales, S., & Edmunds, M. G. 2002, MNRAS, 335, 753
Kölbig, K. S. 1970, Mathematics of Computation, Vol. 24, 111, 679
Kovács, A. 2006, PhD thesis, Caltech
Kovács, A., Chapman, S. C., Dowell, C. D., Blain, A. W., Ivison, R. J., Smail, I., & Phillips, T. G. 2006, ApJ650, 592
Kovács, A. 2008a, Proc. SPIE, 7020, 45
Kovács, A. 2008b, Proc. SPIE, 7020, 5
Krügel, E., Steppe, H., & Chini, R. 1990, A&A, 229, 17
Leeuw, L. L., Robson, E. I. 2009, AJ, 137, 517
Le Floc'h, E., et al. 2005, ApJ, 632, 169
Leong M. M., Peng, R., Houde, M., Yoshida, H., Chamberlin, R, & Phillips, T. G. 2006, Proc. SPIE, 6275, 21
Lonsdale, C. J., et al. 2003, PASP, 115, 897
Lonsdale, C. J., et al. 2009, ApJ, 692, 422 (L09)
Owen, F. N., & Morrison, G. E. 2008, AJ, 136, 1889
Owen, F. N., Morrison, G. E., Klimek, M. D., & Greisen, E. W. 2009, AJ, 137, 4846
Polletta M., et al. 2007, ApJ, 663, 81
Pope, A., et al. 2006, MNRAS, 370, 1185
Press W. H., Flannery B. P., & Teukolsky, S. A. 1986, Numerical Recipes in C: The Art of Scientific Computing (Cambridge: Cambridge Univ. Press)
Seaquist, E., Yao, L., Dunne, L., & Cameron, H. 2004, MNRAS, 349, 1428
Sodroski, T. J., Odegard, N., Arendt, R. G., Dwek, E., Weiland, J. L., Hauser, M. G., & Kelsall, T. 1997ApJ, 480, 173
Tacconi, L. J., et al. 2006, ApJ, 640, 228
Weedman, D., et al. 2006, ApJ, 653, 101
Weiss, A., et al. 2009, ApJ, 707, 1201
Yang, M., PhD thesis, Caltech, 2007
Younger, J. D., et al. 2009, ApJ, 704, 803
Yun, M. S., Reddy, N. A., & Condon, J. J. 2001, ApJ, 554, 803

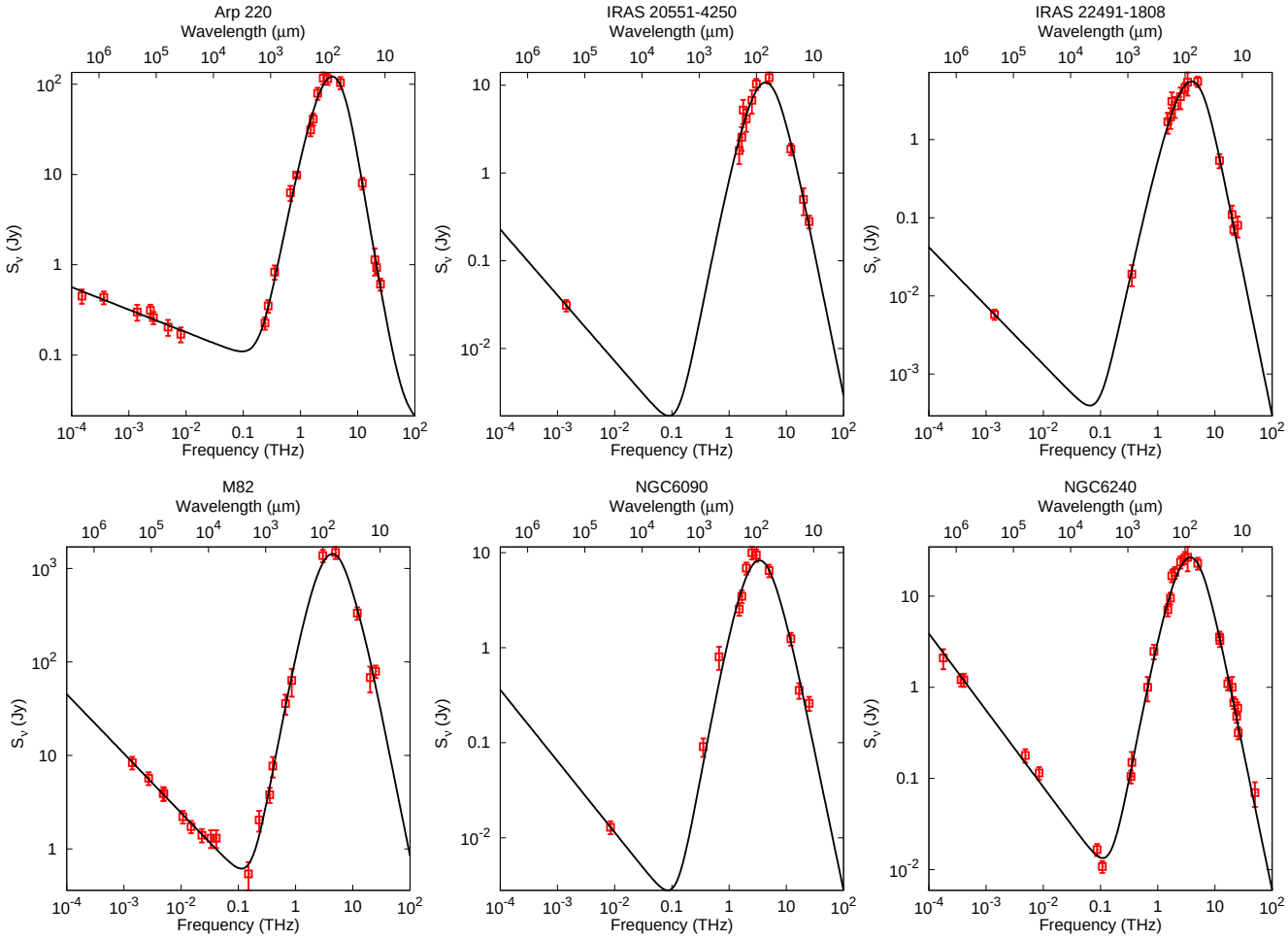

Figure 5. (online only) Individual powerlaw temperature distribution SED fits to the local starbursts. The data used in our analysis are shown with hollow red squares and errorbars. The sources with insufficient radio data assume α=0.75 for the radio spectral index.

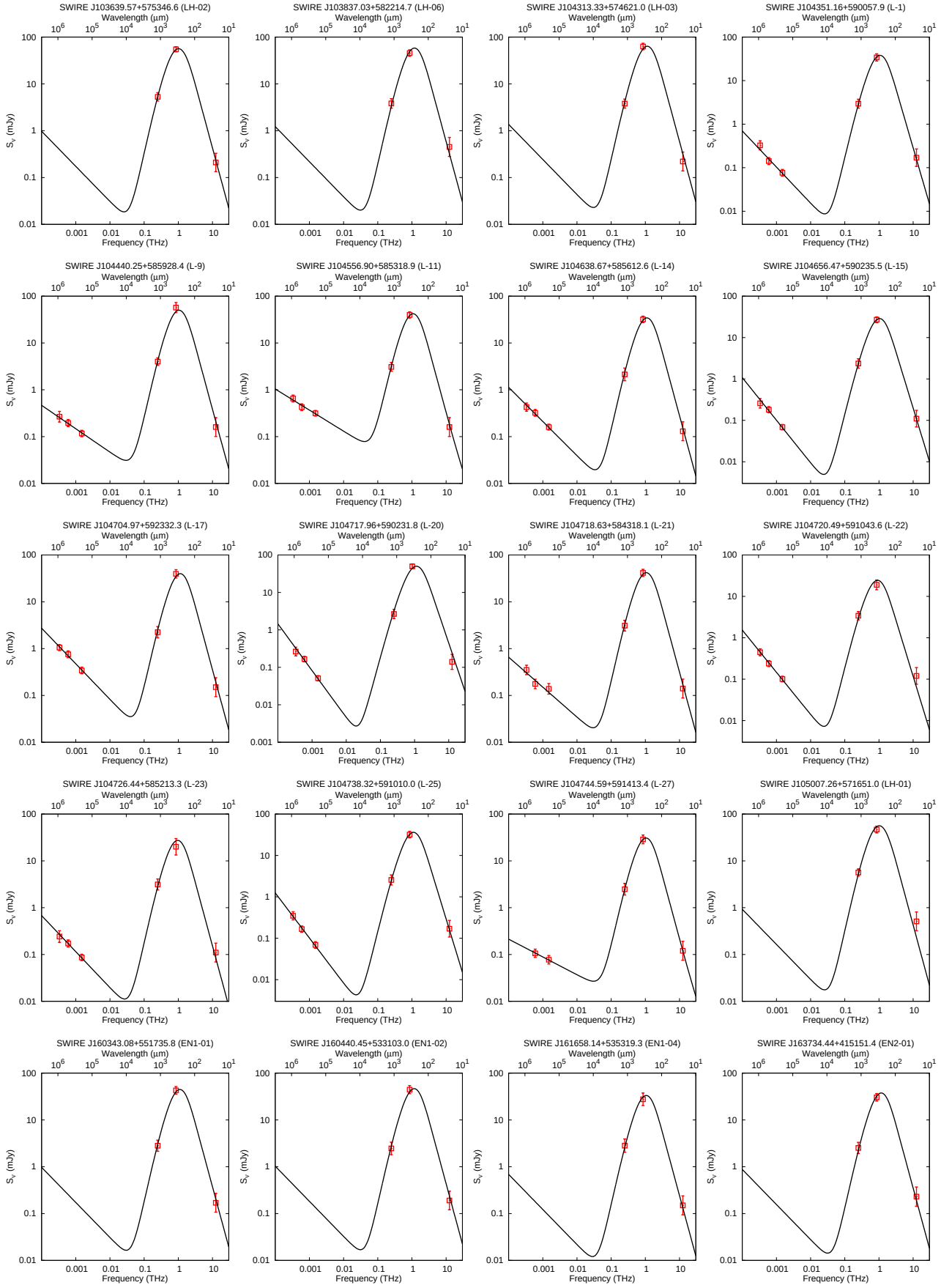

Figure 6. (online only) Individual powerlaw temperature distribution SED fits to our sources. The data are shown with hollow red squares and errorbars. The 24 μm points reflect the expected continuum contribution to the in-band flux-densities, according to Fig. 3, with an uncertainty of 0.25 dex. The sources without radio data assume α=0.75 for the radio spectral index.